Chinese Chemical Letters 34 (2023) 108634

Contents lists available at ScienceDirect

Chinese Chemical Letters

journal homepage: www.elsevier.com/locate/cclet

Layer-by-layer enriching active Ni-N_3C sites in nickel-nitrogen-carbon electrocatalysts for enhanced CO_2-to-CO reduction

Yongqi Ren[a], Ruopeng Chang[a], Xu Hu[a], Junjie Guo[b,*], Guangping Hao[a,*], Anhui Lu[a]

[a] State Key Laboratory of Fine Chemicals, Frontier Science Center for Smart Materials, Liaoning Key Laboratory for Catalytic Conversion of Carbon Resources, School of Chemical Engineering, Dalian University of Technology, Dalian 116024, China
[b] Key Laboratory of Interface Science and Engineering in Advanced Materials, Ministry of Education, Taiyuan University of Technology, Taiyuan 030024, China

ARTICLE INFO

Article history:
Received 19 March 2023
Revised 24 May 2023
Accepted 29 May 2023
Available online 1 June 2023

Keywords:
Porous carbons
Nanocarbons
CO_2 electroreduction
M-N_3C structure
Nonprecious electrocatalysts

ABSTRACT

Transition metal and nitrogen co-doped carbons (M-N-C) have proven to be promising catalysts for CO_2 electroreduction into CO because of the high activity and selectivity. Effective enrichment of the active transition metal coordinated nitrogen sites is desirable but is challenging for a practical volumetric productivity. Herein, we report four kinds of model electrocatalysts to unveil this issue, which include the NC structures with surface N-functionalities, Ni-N-C_I with one layer of surface Ni-N_3C sites, NC@Ni-N-C_I with surface N-functionalities and underneath Ni-N_3C sites as well as Ni-N-C_II with doubled surface Ni-N_3C sites. The X-ray absorption spectroscopy indicates the coordination configuration of Ni-N_3C. For NC catalysts, when N-doping level increased from 3.5 at% to 8.4 at%, the CO partial current density increased from below 0.1 mA/cm^2 to 3 mA/cm^2. Introducing one layer of Ni-N_3C onto the NC structures leads to a 54 times higher CO partial current density than that of NC, in the meantime the FE_{CO} is 66 times higher. Furthermore, doubling the density of surface Ni-N_3C sites by a layer-by-layer method doubles the CO partial current density (j_{CO}), indicating its potential to achieve a high density of active coordinated sites and current densities.

Electrocatalytic reduction of CO_2 (CO_2RR), based on the sustainable energy input (solar-wind-geo-hydro, SWGH), has been regarded as a promising pathway to convert the captured CO_2 into value-added chemicals [1–5]. The products of CO_2RR span from simple C1 products (carbon monoxide (CO) and formic acid) to higher-order multi-electron products including ethanol, *n*-propanol, *etc.* [6,7]. For CO_2-to-CO, typical working catalysts are precious metals (*e.g.*, Au [8], Ag [9]), however limited by their scarcity and high cost for large scale deployment. In recent years, earth-abundant carbon materials with relevant to proper functionalization turn into more appealing catalysts for CO_2RR. There are three major groups including: (1) metal-free heteroatom (B [10], N [11,12], P [13], S [14], *etc.*)-doped carbons, most commonly N-doped type (NC); (2) transition metal (M) and nitrogen (N) co-doped carbons, typically M-N-C type [15–17]; (3) carbon immobilized molecular catalysts [18].

Among these, M-N-C type catalysts are a kind of interesting materials, which not only have the advantages of metal catalysts but also have a low cost. For instance, Su *et al.* reported a novel Ni-N-modified graphene electrocatalysts, Ni-N-Gr that was prepared by the heat treatment of a Ni-N organometallic complex in the presence of graphene oxide [19]. Later on, various transition metals (*e.g.*, Co, Fe, Ni, *etc.*) and nitrogen co-doped carbon-based catalysts were explored for electrochemical reduction CO_2 to CO. Extensive researches were conducted to unveil the nature of the active sites [20,21], which include their coordination details [22,23], the dispersion [24,25] as well as the surface and volumetric density [26].

Porous carbons decorated with Ni-N coordination sites have proven to be particularly active for the reduction of CO_2 to CO [27–29]. For instance, Li *et al.* proposed that Ni-N_4 is the active site proved by EXAFS, which has high selectivity and activity for CO_2 to CO (FE_{CO} of 99% at −0.81 V and current density of 28.6 mA/cm^2) [30]. Similarly, a recent characterization study by Koshy *et al.* indicated that the Ni-N_4 sites are likely the active centers based on the time-of-flight secondary ion mass spectrometry (TOF-SIMS) [31]. The TOF-SIMS technique provided the fragments information of the Ni-N-C catalysts, however, for samples with a low Ni loading (*e.g.*, <1 wt%) lacked featured fragment information [32]. The reported CO_2RR activities vary considerably, and some of which are contradictory. In addition, there also lacks determination of the contri-

* Corresponding authors.
E-mail addresses: guojunjie@tyut.edu.cn (J. Guo), guangpinghao@dlut.edu.cn (G. Hao).

https://doi.org/10.1016/j.cclet.2023.108634
1001-8417/

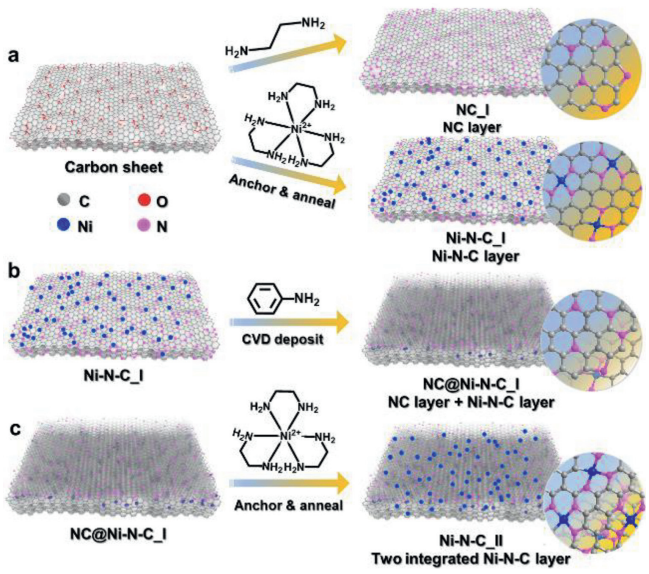

Fig. 1. Schematic illustration of the designed model catalysts based on nanoengineering towards targeted Ni and N-containing functionalities.

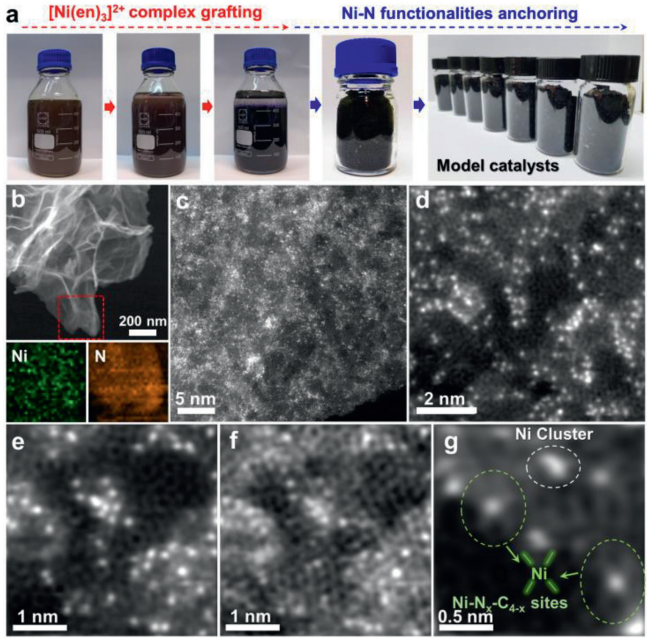

Fig. 2. (a) Typical procedures for the synthesis of Ni-N-C_I catalyst. (b) HAADF-STEM image and the EELS mapping of the Ni-N-C_I. (c–g) Aberration-corrected HAADF-STEM images of Ni-N-C_I under different magnifications.

bution of Ni and N doped C-moieties and pure N-functionalities in Ni-N-C type catalysts.

Moreover, the low concentration of the dispersed Ni-N_x centers in porous carbon matrix is a challenging problem, which calls for effective methods to enrich their surface/volumetric density, and thus for higher current density towards targeted reduction products. Typical strategies to increase active sites include defect-trapping strategy [33], dangling bond trapping strategy [34], chemical chelation strategy [35], and vapor deposition (CVD) strategy [36]. The direct increase of the metal species in the synthesis often causes the migration and agglomeration of the dispersed metals into CO_2RR-inactive nanoparticles.

Herein, we report a family of Ni-N-C catalysts with distinct properties on the dispersion and accessibility of atomically dispersed Ni-N_3C active sites for electrocatalytic CO_2RR. The model catalysts were prepared by nanoengineering of oxidized carbon sheets (CSs), which were subject to different functionalization for targeted active sites (Fig. 1). All the model samples were prepared from the same batch of CSs colloids. For instance, the Ni-N-C catalyst was prepared through the complex-assisted method to simultaneously impart the nitrogen and carbon atoms coordinated nickel active sites. In details, we used the tris(ethylenediamine)nickel(II) complex (denoted Ni(en)$_3$) as the Ni dopants, wherein nickel(II) serves as Lewis acid readily binding six N atoms with lone pair of electrons. The Ni(en)$_3$ anchored CSs was thermally treated, and leached with hydrochloric acid subsequently, resulting in the Ni-N-C materials (Ni-N-C_I, Fig. 1a). In parallel, replacing of Ni(en)$_3$ with en would lead to the formation of N-doped carbons (NC_I). We further coated the Ni-N-C_I materials with a thin layer of nitrogen doped carbon through a known aniline CVD process [37]. By doing so, the model catalysts of NC-t@Ni-N_C (where t indicates the CVD time) were obtained, which featured the shielded coordinated Ni sites (Fig. 1b). Furthermore, we re-imparted the coordinated Ni sites on the NC-120@Ni-N_C samples by using the same Ni(en)$_3$-assisted method, aiming to double the density of coordinated Ni sites (Ni-N-C_II, Fig. 1c, details can be found in Supporting information). In addition, we measured the thickness of Ni-N-C layer on Ni-N-C_I using atomic force microscopy (AFM) technique. The thickness of the pristine carbon nanosheets is 4.3 ± 0.6 nm (Figs. S1a and b in Supporting information). After CVD treatment, the resultant sample of NC-120@Ni-N-C_I show the thickness of 13.3 ± 2.1 nm (Figs. S1c and d in Supporting information). Accordingly, the thickness of Ni-N-C layer on both sides can be determined to be around 9 nm.

Structural characterizations were carried out to determine the physicochemical features of the three groups of model catalysts. In the XRD patterns, only a broad peak at approximately 25° was detected, suggesting that the Ni-species were in a highly dispersed state (Fig. S2 in Supporting information). Based on N_2 adsorption isotherms (Fig. S3 in Supporting information), the specific surface area (S_{BET}) of the Ni-N-C_I catalyst was determined to be 188 m^2/g, which is very close to its NC counterpart (189 m^2/g). Deposition of a thin NC layer onto Ni-N-C_I catalyst led to a reduced S_{BET} of 124 and 115 m^2/g for NC-10@Ni-N_C and NC-120@Ni-N_C, respectively. This is likely because the deposition thermodynamically prefers at the defect sites, *e.g.*, nano-pore or edge sites, and thus lowers the detectable S_{BET} (Fig. S3).

The schematic of Ni-N-C catalysts was shown in Fig. 2a. The dispersion of Ni species was studied by high-angle annular dark field scanning transmission electron microscopy (HAADF-STEM, Fig. 2b) and transmission electron microscopy (TEM, Fig. S4 in Supporting information). The Ni and N species were detected to be evenly dispersed (Fig. 2b, below). By using the HAADF-STEM technique (Figs. 2c–g), the bright dots are observed that are relevant to the Ni atoms in atomically dispersed state (Fig. 2c). In more details, the dispersed Ni species are predominately binding to the edge sites of the randomly stacked graphene layers; in contrast, the density of the Ni atoms is much lower on the basal plane (Fig. 2d). This phenomenon aligns with the findings of previous reports [38]. Upon further magnifying, one can see that the Ni species mainly exist as coordinated Ni centers, 2 Å in Ni-N_x or tiny Ni clusters 4–5 Å (Figs. 2e–g). The single atom or cluster of Ni species were assessed by analysis of the STEM images using Nano Measurer 1.2 software. The average statistical results reveal that 74% of the bright dots are attributed to single Ni coordinated N and C-sites, while 26% are associated with metallic Ni clusters (Table S1 in Supporting information).

Furthermore, the chemical environments of coordinated Ni centers of a typical catalyst were investigated by the X-ray absorp-

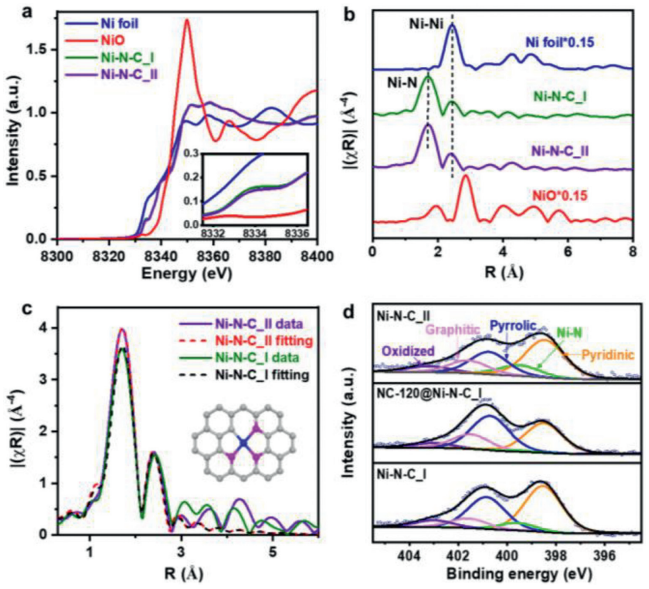

Fig. 3. Electronic states of Ni atom and chemical state of surface N-functionalities in this series of catalysts. (a) Ni K-edge XANES profiles of Ni-N-C_I, Ni-N-C_II as well as Ni foil and NiO benchmarks, inset shows the expanded pre-edge region. (b) Corresponding Fourier transforms spectra. (c) Fittings results of Ni-N-C_I and Ni-N-C_II. (d) XPS spectra comparison in N 1s region.

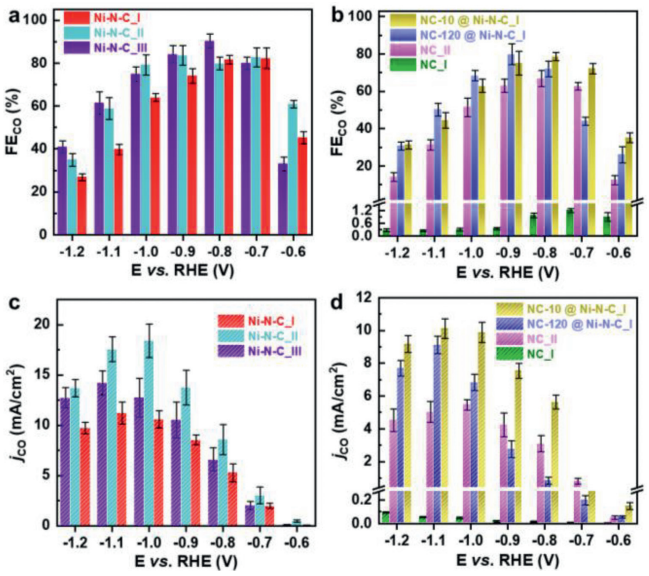

Fig. 4. CO_2RR evaluation results on NC, Ni-N-C and NC layer coated Ni-N-C counterparts. (a, b) FE_{CO} at varied applied potentials in the H-cell, E *vs.* RHE. (c, d) Corresponding CO partial current density (j_{CO}) for this family of model catalysts.

tion spectroscopy (XAS). The X-ray absorption near-edge structure (XANES) spectra displayed the peaks at 8340 eV of the $1s \rightarrow 4p_z$ transitions, which are evident on the Ni-N-C samples than benchmarks of Ni foil and NiO. The position of the rising edge of Ni-N-C was found to fall between that of Ni foil and NiO (Fig. 3a). Hence, the valence of the Ni atoms ($Ni^{\delta+}$) in the coordinated states should be $0 < \delta < 2$. We further conducted Electron Paramagnetic Resonance (EPR) measurements at 100 K to track the unpaired electron in Ni atoms (Fig. S5 in Supporting information). However, no signals were obtained. Thus, the existence of unsaturated $Ni^{\delta+}$ could be excluded. Therefore, we speculated this was caused by the co-existence of two forms of Ni species: (1) coordinated Ni atoms showing +2 valance states, (2) metallic Ni clusters with 0 valance state. Notably, the characteristic peak at 8340 eV observed in our samples is consistent with the nickel phthalocyanine (Ni(II)Pc) with square planar coordinated $Ni-N_4$, as reported in previous studies [39,40]. Similarly, the peaks at 8352 and 8358 eV that are relevant to the $1s \rightarrow 4p_xp_y$ transitions and multiple scattering processes, coinciding with the reported results on Ni(II)Pc. However, the intensity was reduced, likely due to the distorted geometry and/or the mixed coordinating environment of Ni to neighbored N or C atoms [40].

We also collected the Ni K-edge extended X-ray absorption fine structure (EXAFS) spectra to identify the coordination environment of the Ni atoms in Ni-N-C. The Fourier transformed EXAFS spectra showed that the weak peak at 2.1 Å was ascribed to Ni-Ni interaction (Fig. 3b) [41]. By combining the above XRD and HAADF-STEM results, it can be concluded that the Ni-Ni interaction is associated with the formation of small Ni clusters. The main sharp peak at *ca.* 1.38 Å was stemmed from the scattering interaction between the Ni atoms and the first shell ($Ni-N_x$) [42,43]. The fitting results of the EXAFS curves suggest that each Ni site is bonded to 2.4~2.6 N atoms. Based on the XAS characterization, high-resolution XPS spectra as well as the previous findings on the identification of the nickel-coordinated nitrogen centers [25,41,44,45]. We speculate that the active coordinated sites are likely to be $Ni-N_3C$ (Fig. 3c).

The surface chemical composition and elemental states of NC, Ni-N-C, and NC-t@Ni-N_C were studied by X-ray photoelectron spectroscopy (XPS) (Fig. 3d and Table 1). The surface Ni content for Ni-N-C_I was 0.56 at%. After coating a layer of NC, the surface Ni content reduced to 0.26 at% for the sample of NC-120@Ni-N-C_I. This indicated that *ca.* 54% of Ni sites were covered by the NC layer, being undetectable by XPS. In contrast, 10 min CVD process barely affected the detectable surface Ni species, *i.e.*, 0.56 *vs.* 0.55 at% before and after 10-min deposition (Fig. S6 in Supporting information). In contrast, the secondary functionalization with $Ni(en)_3$ on NC-120@Ni-N-C resulted in a further increase in its Ni contents to 0.72 at%, indicating a 1.3 times higher density of surface Ni sites. Meanwhile, we determined the overall compositions by elemental analysis (Table 1), which showed a similar trend as the XPS results.

The fitted high-resolution N 1s spectra for all samples revealed the presence of prominent pyridinic (~398.4 eV) and pyrrolic-N (~400.6 eV), together with the graphitic-N (~401.5 eV), and oxidized N (N-ox ~403.2 eV) species (Fig. 3d and Fig. S7 in Supporting information) [46]. Upon doping with Ni species, the Ni-N-C catalysts evidenced the emerging of $Ni-N_x$ moieties (~399.7 eV). Depositing a thin NC layer onto Ni-N-C catalysts by CVD for 10 min slightly reduced the $Ni-N_x$ proportion, however, a 120-min long deposition rendered the surface state more like pure NC. Another interesting feature is the clear reduction of pyrrolic-N fraction (from 1.61 at% to 0.99 at%) but the increase of the total surface-N contents (from 3.98 at% to 4.17 at%) upon coordinating with Ni species (Tables S2 and S3 in Supporting information). It is reasonable to believe that the re-arrangement of N functionality is induced by the introduction of Ni species, likely forming the thermodynamically more stable $Ni-N_3$ moieties [47,48]. It also identified that the pyrrolic-N played a crucial role in the above re-arrangement [49].

Next, we investigated the CO_2 reduction performances of the three model catalysts. Liner sweep voltammetry (LSV) saturated electrolytes than Ar-saturated for all the catalysts (Fig. S8 in Supporting information). Both the recorded current density and the onset potential coincides similar trend, indicating the activity orders: Ni-N-C > NC-10@Ni-N-C > NC-120@Ni-N-C > NC. The challenging issue is that the community lies in how to quantitatively determine the contribution that each type of active site offers [49,50]. We thoroughly investigated the product distribution after stationary electrolysis at each applied potential for 1 h (Figs. 4a and

Table 1
Elemental composition in the surface and bulk region of this family of model catalysts.

Model	Sample	Surface region composition (at%)[a]				Bulk phase composition (at%)[b]		
		Ni	N	C	N/Ni	Ni[c] (wt%)	N	C
Group 1	Ni-N-C_I	0.56	4.10	92.95	7.32	0.45	4.92	88.76
	Ni-N-C_II	0.72	4.17	92.11	5.79	0.52	3.80	82.75
Group 2	NC_I	–	3.00	89.76	–	–	5.22	89.25
	NC_II	–	8.45	83.00	–	–	10.20	72.50
Group 3	NC-10@Ni-N-C_I	0.55	3.78	92.52	6.87	0.43	4.60	84.32
	NC-120@Ni-N-C_I	0.26	3.98	94.18	15.30	0.42	4.27	86.94

[a] Based on XPS survey spectra in Fig. S6.
[b] Based on elemental analysis except Ni.
[c] Ni content was based on ICP-MS results.

b, Fig. S9 in Supporting information). Over all the catalysts, the detected products are CO and H_2, accounting for a total unit FE. For clarity, we also confirmed the used electrolyte by ^{1}H NMR, which excluded the formation of any liquid products.

We first checked the reliability of the collected data by taking the typical electrocatalyst of Ni-N-C_II as the example. The presented results are the average of three repeated experiments, and the error bar was plotted using the standard deviation for three repeated experiments (Fig. S10 in Supporting information). As shown, it shows quite good reproducibility. In the following, we follow the same measurement procedure and evaluated the CO_2RR performances. Fig. 4a showed the FE_{CO} for Group 1 catalysts which have direct N coordinated Ni sites. The catalyst Ni-N-C_I reached the highest FE_{CO} of *ca.* 80% at −0.7 V *vs.* RHE. The value is 10%−15% lower than that of the reported single atom catalysts (normally FE_{CO} > 90%) [51], but precisely reflect its structural features that composed of 74% single Ni coordinated N and C-sites and 26% metallic Ni clusters (Table S1 and Fig. S11 in Supporting information). The 26% Ni clusters are believed to preferably favor the hydrogen evolution reaction (HER), contributing a FE_{H2} of 20% (Fig. S12 in Supporting information). To confirm this issue, we further extensively re-leached our Ni-N-C_I sample for prolonged time (5 days), in order to reduce the fraction of Ni clusters of Ni-N-C_III. As expected, its FE_{CO} indeed reached 90.3% at −0.8 V *vs.* RHE. We compared the catalytic performance with the atomically dispersed Ni-N-C electrocatalysts in Table S4 (Supporting information), which showed comparable activity with previous observations [32,52]. The Ni-N-C_II with 1.3 times more Ni sites showed similar FE_{CO} as that of Ni-N-C_I, indicating the identical nature of active sites.

The current density, governed by the density of active sites, is a key parameter for practical applications [53]. The CO partial current densities (j_{CO}) of Group 1 catalysts were plotted in Fig. 4c. The current densities reached a plateau when potentials reached in the range of −1.0 ∼ −1.1 V *vs.* RHE, then started to decrease due to the competitive HER reaction. Intriguingly, the Ni-N-C_II with 1.3 times more Ni sites led to a consistent increase of j_{CO} by 52% to 74% in the kinetic region of −0.7 ∼ −1.0 V *vs.* RHE. We further calculated the electrochemical specific surface areas from the double-layer capacitance (C_{dl}). Although the specific surface area of Ni-N-C_II is smaller than that of Ni-N-C_I. However, the electrochemical specific surface area (ECSA) of Ni-N-C_I and Ni-N-C_II was very close with the value of 0.50 and 0.55 mF/cm^2, respectively (Fig. S13 in Supporting information), which is probably due to the presence of higher density of active sites on the Ni-N-C_II. We also compared the TOF of different model carbon materials at different potential. The high-density of coordinated Ni-N_3C centers led to the superior TOF (Fig. S14 in Supporting information). For instance, Ni-N-C_II shows the highest TOF of 674.4 h^{-1} at −1.0 V *vs.* RHE.

The results revealed that transforming the N-doped carbon layer into the second Ni-N_3C layer effectively enhanced the reduction activity of CO_2-to-CO. The layer-by-layer enriching strategy enabled a spatial dispersion of the atomically dispersed Ni-species, and thus avoided its agglomeration to bigger nanoparticles. It could further improve the spatially enriching efficiency if the N-doped layer can be engineered for efficiently anchoring Ni-sites. Alternatively, removal of metallic clusters (Ni-N-C_III) also resulted in the enhancement j_{CO} by 20%−31% in the applied potential range (Fig. 4c).

For Group 2 catalysts of pure N-doped carbons, the total surface N content in NC_I is 3.58 at%, while on NC_II prepared by replacing the ethylenediamine by dipyridyl, it is 2.4 times higher. Interestingly, the 2.4 times higher N content led to a marked enhancement on the catalytic performance. Over NC_II, nearly 60–200 times higher FE_{CO} was observed in the potential range of −0.6 ∼ −1.2 V *vs.* RHE as compared to NC_I (Fig. 4b). The detailed N 1s spectra revealed that the pyridinic-N and pyrrolic-N in NC_II was most increased by 170% and 178%, respectively (Tables S2 and S3). The largest increment of pyridinic-N and pyrrolic-N was likely relevant to the enhancement of the selectivity towards CO, and thus their j_{CO} (Fig. 4d) [54]. Moreover, the j_{CO} for NC_I was negligible, while the catalyst of NC_II delivered much higher j_{CO}, reaching the highest point of 5.5 mA/cm^2 at −1.0 V *vs.* RHE. Overall, over N-doped carbon catalysts, we find the obvious disproportions between both the FE_{CO} and j_{CO} and the increased density of N functionalities. Thus, we speculate that for N-doped catalysts, a threshold of the density of active sites exists, beyond which their activity is enhanced largely.

Subsequently, we investigated Group 3 catalysts with indirect N coordinated Ni sites (Fig. 4b). For NC-10@Ni-N-C_I with thinner NC coating, its selectivity trend followed that of the original Ni-N-C_I. For NC-120@Ni-N-C_I with thicker NC coating, at lower potential (−0.6 and −0.7 V *vs.* RHE), its FE_{CO} was roughly half of that Ni-N-C_I. While the FE_{CO} reached the same level at −0.8 V and outperformed Ni-N-C_I when the electrode potential was reached −0.9 V *vs.* RHE and above. For instance, at potentials of −1.0 and −1.1 V *vs.* RHE, its FE_{CO} increase by 10% and 25% as compared to Ni-N-C_I. While the j_{CO} of Group 3 sits well in between Group 1 and Group 2.

We conducted the *in-situ* ATR-SEIRAS measurement to analyze the changes of intermediates for Ni-N-C materials during CO_2RR (Fig. 5). *In-situ* ATR-SEIRAS was performed in the 0.5 mol/L $KHCO_3$ at the potential range of −0.1 ∼ −1.2 V *vs.* RHE. The small peaks at 1445 and 2086 cm^{-1} could be assigned to *COOH and *CO, which are the key intermediates for CO_2 reduction to CO [55]. Besides, as the overpotential increasing, the peak of CO_3^{2-} at 1395 cm^{-1} was found to be more intense. This result suggested that the hydrogen evolution reaction (HER) of Ni-N-C_I with cluster is more severe compared to Ni-N-C_III, leading to the increased consump-

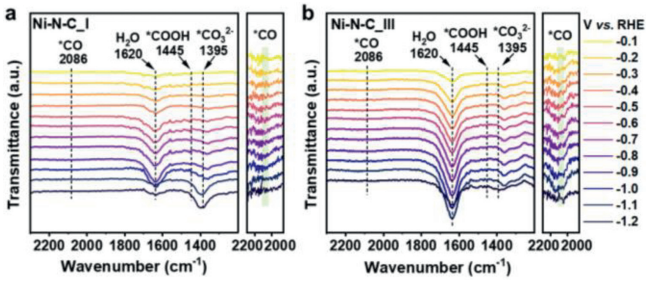

Fig. 5. *In-situ* ATR-SEIRAS spectra of (a) Ni-N-C_I and (b) Ni-N-C_III. The range from 2110 cm^{-1} to 2020 cm^{-1} is highlighted.

tion of H^+. As a result, an excess of OH^- is produced and combines with CO_2, which causes the saturation buffer equilibrium of CO_2 towards the formation of CO_3^{2-} [56]. The above results also provide evidences for confirming the Ni-N_3C active sites for CO_2 reduction to CO.

To get in-depth understanding in the activity trend and N- and Ni-containing functionalities' contribution to the current density, we correlated different active sites with their FE_{CO} and S_{BET} normalized j_{CO} (Fig. 6). In this section, the j_{CO} refers to the normalized j_{CO} values normalized by S_{BET}. The FE_{CO} in our work reflects the nature of active sites for CO_2-to-CO, while the j_{CO} is the indicator of the density of active sites contributing to the current for CO_2-to-CO intrinsically. First, we correlated the FE_{CO} and j_{CO} of Group 1 and Group 3. Overall, the catalysts of Group 1 with direct Ni-N_3C sites showed higher and constant FE_{CO} than that of Group 3 with indirect Ni-N_3C sites. At −0.7 V *vs.* RHE, Group 1 displayed relatively constant FE_{CO} at *ca.* 80%. For Group 3, a thinner NC coating was rather dominated by the Ni-N_3C sites, and thus delivered a very close FE_{CO} to that of direct Ni-N_3C sites. While, the one with thicker NC coatings showed the most indirect Ni-N_3C sites, exhibiting only half of FE_{CO}. We estimated their contribution to the j_{CO} by calculating their slopes of the linear fitting. The direct Ni-N_3C sites were observed to contribute 14.2 times higher than the indirect Ni-N_3C sites.

At middle potential (−0.9 V *vs.* RHE), both the direct and indirect Ni-N_3C sites led to a *ca.* 80% FE_{CO}, indicating a similar overall activity for Group 3. Surprisingly, the slope of Group 3 was even higher than that of Group 1. We speculated that the NC coating created a confined effect for the covered Ni-N_3C sites that enhanced their activity in catalyzing CO_2-to-CO or suppressing the competitive HER.

At high potential (−1.1 V *vs.* RHE), the FE_{CO} decreased for all the catalysts, while the j_{CO} continued to increase. The reduction of FE_{CO} was due to the increasingly competitive HER, which attracted half of the transferred electrons. For the linear fitting of j_{CO}, the slope of Group 1 is 1.5 times higher than that of Group 3. This revealed, at potential of −1.1 V, the direct Ni-N_3C coordinated sites were more catalytically active for CO_2-to-CO than the indirect type.

Similarly, we then moved to the correlation between the FE_{CO} and j_{CO} with the surface atomic Ni sites of Group 1 and Group 3. Overall, the trend was like the above correlation. However, the slope of j_{CO} plot correlated to the Ni sites was lower as compared to the correlation with the Ni-N_3C sites. This was because of the existence of metallic Ni clusters that were HER active. For instance, at −1.1 V, the slope of j_{CO} plot was reduced by 66.2% and 41.3% for Group 3 and Group 1, respectively. Finally, the relationship between the FE_{CO} and j_{CO} and the typical N-functionality of pyridinic-N was plotted. On Group 3, we did not observe positive effects of the existence of pyridinic-N in contributing CO_2-to-CO. The higher pyridinic-N content, however, resulted in the lower j_{CO}. In other word, this revealed the dominated role of the Ni-N_3C coordinated sites in CO_2-to-CO for Ni-N-C type catalysts. We can further quantitatively analyze their contributions by comparing their corresponding slopes. A S1/S2 of 116.67, 34.48 and 80.53 was obtained at −0.7, −0.9 and −1.1 V *vs.* RHE, respectively. This provided clear clues on the understanding of their activity, and a valuable method for creating high density active sites to enhance the current density for CO_2-to-CO.

A large set of control experiments combined with aberration-corrected HAADF-STEM images, XAS characterization as well as the *in-situ* ATR-SEIRAS spectra were applied to identify dispersed Ni-N_3C sites that are likely the active centers for CO_2 reduction to CO. For instance, increasing leaching cycles promoted activity by exposing more coordinated Ni-N_3 sites. This observation was consistent with previous studies on Ni-N-C materials [57]. In addition, quantification of Ni species showed that 74% of the sample consisted of single Ni-coordinated N sites, while 26% were metallic Ni clusters for Ni-N-C_I. The correlation between CO selectivity and

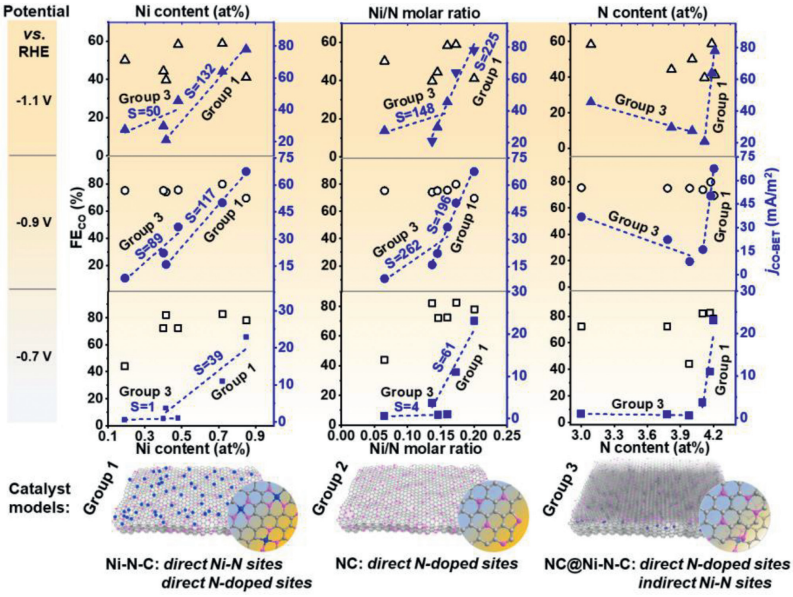

Fig. 6. The correlation (top) between key structural parameters and core performance indexes on this family of functional carbon-based model catalysts (below).

metal entities revealed that FE_{CO} was 10%−15% lower than that of samples dominated by single Ni sites, supporting the proposed N-coordinated Ni active sites [58,59].

Besides, considering the oxidized carbon sheet as the support to fabricate this series of electrocatalysts, we also carefully analyze the effects of O atom on catalytic performance. The previous literatures reported that the axial O atoms in coordinated Ni-N_4-O structures can induce an axial traction effect, which promote the CO_2 reduction [60]. However, in principle, it is unlikely to form the axial O atoms by introducing the nickel nitrate and ethylenediamine complex into the support in our work. Anther evidence is that the O contents of this family of electrocatalyst are rather close. Only after introducing the metal species, the remarkably increased CO partial current density can be observed. These results suggested that the presence of O atoms should not play evident role in CO_2RR.

In summary, a family of Ni and N functionalized carbon electrocatalysts were developed through a nickel-diamine complex-assisted nanoengineering method. By correlating the structural features and their CO_2RR performances, we explored the roles of specific functionalities which were responsible for catalyzing CO_2-to-CO conversion. A tiny amount of surface Ni-N_3C active species significantly enhance of the CO partial current density, which was nearly 50 times higher than that of the N-doped sites. Technically important, the increase of j_{CO} was achieved by a layer-by-layer enriching strategy, in which the density of Ni-N_3C coordinated sites was increased nearly linearly. Our results may inspire the new design and fabrication of advanced nonprecious metal catalysts for other heterogeneous reactions beyond the target in this work.

Declaration of competing interest

The authors declare that they have no known competing financial interests or personal relationships that could have appeared to influence the work reported in this paper.

Acknowledgments

This work was financed by National Natural Science Foundation of China (Nos. 22275027, 21975037), the Fundamental Research Funds for the Central Universities (Nos. DUT22LAB607, DUT22QN206). We also thank Prof. Si from Chinese Academy of Sciences for his support in the collection and analysis of the XAS data.

Supplementary materials

Supplementary material associated with this article can be found, in the online version, at doi:10.1016/j.cclet.2023.108634.

References

[1] M. Rahimi, A. Khurram, T.A. Hatton, et al., Chem. Soc. Rev. 51 (2022) 8676–8695.
[2] J. Liu, C. Chen, K. Zhang, et al., Chin. Chem. Lett. 32 (2021) 649–659.
[3] S. Jin, Z. Hao, K. Zhang, et al., Angew. Chem. Int. Ed. 60 (2021) 20627–20648.
[4] Z. Gao, J. Li, Z. Zhang, et al., Chin. Chem. Lett. 33 (2022) 2270–2280.
[5] T. He, A.R. Puente-Santiago, S. Xia, et al., Adv. Energy Mater. 12 (2022) 2200493.
[6] B. Zhang, Y. Jiang, M. Gao, et al., Nano Energy 80 (2021) 105504.
[7] F. Wang, W. Zhang, H. Wan, et al., Chin. Chem. Lett. 33 (2022) 2259–2269.
[8] S. Li, A.V. Nagarajan, D.R. Alfonso, et al., Angew. Chem. Int. Ed. 60 (2021) 6351–6356.
[9] L. Wei, H. Li, J. Chen, et al., ACS Catal. 10 (2020) 1444–1453.
[10] J. Zhao, Z. Chen, J. Zhao, J. Mater. Chem. A 7 (2019) 4026–4035.
[11] P. Yao, Y. Qiu, T. Zhang, et al., ACS Sustain. Chem. Eng. 7 (2019) 5249–5255.
[12] C. Li, Y. Wang, N. Xiao, et al., Carbon 151 (2019) 46–52.
[13] T. Liu, S. Ali, Z. Lian, et al., J. Mater. Chem. A 6 (2018) 19998–20004.
[14] F. Pan, B. Li, W. Deng, et al., Appl. Catal. B: Environ. 252 (2019) 240–249.
[15] J. Gu, C. Hsu, L. Bai, et al., Science 364 (2019) 1091–1094.
[16] L. Dong, X. Hu, Y. Du, et al., J. Mater. Chem. A 9 (2021) 17821–17829.
[17] W. Ju, A. Bagger, G. Hao, et al., Nat. Commun. 8 (2017) 944.
[18] P. Wang, T. Li, Q. Wu, et al., ACS Nano 16 (2022) 17021–17032.
[19] P. Su, K. Iwase, S. Nakanishi, et al., Small 12 (2016) 6083–6089.
[20] W. Wang, L. Shang, G. Chang, et al., Adv. Mater. 31 (2019) 1808276.
[21] S. Shen, C. Han, B. Wang, et al., Chin. Chem. Lett. 33 (2022) 3721–3725.
[22] H. Cheng, X. Wu, X. Li, et al., Chem. Eng. J. 407 (2021) 126842.
[23] B. Lu, Q. Liu, S. Chen, ACS Catal. 10 (2020) 7584–7618.
[24] H. Li, K. Gan, R. Li, et al., Adv. Funct. Mater. 33 (2023) 2208622.
[25] Y. Li, N.M. Adli, W. Shan, et al., Energy Environ. Sci. 15 (2022) 2108–2119.
[26] Y. Lu, H. Wang, P. Yu, et al., Nano Energy 77 (2020) 105158.
[27] F. Pan, H. Zhang, K. Liu, et al., ACS Catal. 8 (2018) 3116–3122.
[28] X. Zhao, Y. Liu, J. Am. Chem. Soc. 142 (2020) 5773–5777.
[29] X. Fu, P. Zhang, T. Sun, et al., Small 18 (2022) 2107997.
[30] X. Li, W. Bi, M. Chen, et al., J. Am. Chem. Soc. 139 (2017) 14889–14892.
[31] D.M. Koshy, A.T. Landers, D.A. Cullen, et al., Adv. Energy Mater. 10 (2020) 2001836.
[32] Y. Gong, L. Jiao, Y. Qian, et al., Angew. Chem. Int. Ed. 59 (2020) 2705–2709.
[33] Z. Liu, S. Li, J. Yang, et al., ACS Nano 14 (2020) 11662–11669.
[34] Y. Qu, L. Wang, Z. Li, et al., Adv. Mater. 31 (2019) 1970316.
[35] Z. Miao, X. Wang, M. Tsai, et al., Adv. Energy Mater. 8 (2018) 1801226.
[36] S. Liu, M. Wang, X. Yang, et al., Angew. Chem. Int. Ed. 59 (2020) 21698–21705.
[37] D. De Fazio, D.G. Purdie, A.K. Ott, et al., ACS Nano 13 (2019) 8926–8935.
[38] K. Huang, Z. Wei, J. Liu, et al., Small 18 (2022) 2201139.
[39] W. Bi, X. Li, R. You, et al., Adv. Mater. 30 (2018) 1706617.
[40] C. Yan, H. Li, Y. Ye, et al., Energy Environ. Sci. 11 (2018) 1204–1210.
[41] Q. Fan, P. Hou, C. Choi, et al., Adv. Energy Mater. 10 (2020) 1903068.
[42] K. Mou, Z. Chen, X. Zhang, et al., Small 15 (2019) 1903668.
[43] R. Daiyan, X. Zhu, Z. Tong, et al., Nano Energy 78 (2020) 105213.
[44] C. Zhao, X. Dai, T. Yao, et al., J. Am. Chem. Soc. 139 (2017) 8078–8081.
[45] S. Gong, W. Wang, R. Lu, et al., Appl. Catal. B: Environ. 318 (2022) 121813.
[46] R. Ge, L. Dong, X. Hu, et al., Chem. Eng. J. 438 (2022) 135500.
[47] C. Wen, F. Mao, Y. Liu, et al., ACS Catal. 10 (2020) 1086–1093.
[48] P. Prslja, N. López, ACS Catal. 11 (2021) 88–94.
[49] T. Asset, S.T. Garcia, S. Herrera, et al., ACS Catal. 9 (2019) 7668–7678.
[50] R. Daiyan, W.H. Saputera, H. Masood, et al., Adv. Energy Mater. 10 (2020) 1902106.
[51] T. Zheng, K. Jiang, N. Ta, et al., Joule 3 (2019) 265–278.
[52] C. Lu, J. Yang, S. Wei, et al., Adv. Funct. Mater. 29 (2019) 1806884.
[53] B. Chen, B. Li, Z. Tian, et al., Adv. Energy Mater. 11 (2021) 2102152.
[54] R.M. Yadav, Z. Li, T. Zhang, et al., Adv. Mater. 34 (2022) 2105690.
[55] M. Huang, B. Deng, X. Zhao, ACS Nano 16 (2022) 2110–2119.
[56] C. Liu, Y. Wu, K. Sun, et al., Chem 7 (2021) 1297–1307.
[57] A.S. Varela, N. Ranjbar Sahraie, J. Steinberg, et al., Angew. Chem. Int. Ed. 54 (2015) 10758–10762.
[58] D.M. Koshy, S. Chen, D.U. Lee, et al., Angew. Chem. Int. Ed. 59 (2020) 4043–4050.
[59] Z. Li, D. He, X. Yan, et al., Angew. Chem. Int. Ed. 59 (2020) 18572–18577.
[60] X. Wang, Y. Wang, X. Sang, et al., Angew. Chem. Int. Ed. 60 (2021) 4192–4198.